Materials Today: Proceedings 38 (2021) 809–815

Contents lists available at ScienceDirect

Materials Today: Proceedings

journal homepage: www.elsevier.com/locate/matpr

Photocatalytic degradation of Rhodamine dyes using zinc oxide nanoparticles

D. Dodoo-Arhin [a,*], T. Asiedu [a], B. Agyei-Tuffour [a], E. Nyankson [a], D. Obada [b], J.M. Mwabora [c]

[a] Department of Materials Science and Engineering, University of Ghana, Ghana
[b] Department of Mechanical Engineering, Ahmadu Bello University, Zaria, Nigeria
[c] Department of Physics, University of Nairobi, Kenya

ARTICLE INFO

Article history:
Received 25 March 2020
Received in revised form 18 April 2020
Accepted 22 April 2020
Available online 28 May 2020

Keywords:
ZnO
Photocatalyst
Sol-gel
X-ray diffraction (XRD)
Rhodamine B
Calcination
Nanoparticles

ABSTRACT

This paper presents the synthesis of nanocrystalline zinc oxide (ZnO) particles via the sol-gel method using zinc acetate as precursor. The calcination temperature of the ZnO was varied to determine its effect on particle size. The resultant samples were characterized using X-Ray Diffraction (XRD), Fourier Transform Infrared (FTIR), UltraViolet–visible Spectroscopy (UV–Vis) and Scanning Electron Microscopy (SEM). Nanocrystalline wurtzite ZnO particles were produced with crystallite size ranging from ~16 nm to ~30 nm. Energy Band gap of the synthesized zinc oxide nanoparticles decreased with increasing calcination temperature and crystallite size. SEM Micrographs showed rice-like microstructure morphology of ZnO nanoparticles. The usage of the ZnO nanoparticles as a photocatalyst was also explored in the degradation of Rhodamine B dye using UV – light with particular attention to the effect of particle size and catalyst load on the degradation efficiency of the dyes. The nanoparticles calcined at 400 °C with crystallite size of 16 nm resulted in the highest degradation efficiency of ~95.41% when 0.2 g catalyst loading was applied.

Selection and peer-review under responsibility of the scientific committee of the International Symposium on Nanostructured, Nanoengineered and Advanced Materials.

1. Introduction

Improper disposal of residual dyes and dye effluent into water bodies by some industries and local textile manufacturers has become a major contributor to the pollution of water bodies in recent times [1]. These pose enormous threat to humans, livestock and the aquatic ecosystem due to their carcinogenic tendencies and poor biodegradability [2]. Particular attention has been paid to organic dyes as major environmental pollutants due to their non-biodegradability and harmful effects on humans owing to their high potential of been carcinogenic [3,4]. Moreover, they have deteriorating effect on the nature and quality of water, and also impede the permeation of sunlight to the detriment of photosynthetic aquatic plants. For instance, traces of organic dyes such as Methylene blue (MB) in water can result in ailments such as abdominal disorders, irritations, anemia as a result of hemolysis and many more [4]. However, the use of this dye is very vital to the making of textile products in the industry especially in dying of fabrics [5]. An annual estimation on the production and use of dyes and pigments worldwide reveals that more than 10,000 dyes and pigments are used and $\sim 7 \times 10^5$ tons are produced synthetically [6] which is an indication that the use of these dyes cannot be avoided because they form an integral part of industrial operations of especially textile and paper industries. Therefore, there is the need to inhibit the harmful effects of these dyes on the ecosystem. Over the years, studies have been done to reclaim dye-polluted water using water treatment techniques such as adsorption, coagulation and membrane separation [7]. The techniques however, only enhanced the conversion of the pollutants in the water into the solid phase resulting in the generation of secondary pollutants which may equally have adverse effects on the ecosystem [8]. This calls for a much effective and safe method of removing the dyes without the generation of secondary harmful products.

In view of this, degradation of dyes dissolved in water via photocatalysis using semiconductor nanoparticles as photocatalyst has been explored in recent times for the removal and reclamation of dye polluted water bodies and has gained much interest in this regard [9]. The technique is highly beneficial and safe as it is suit-

* Corresponding author.
E-mail address: ddodoo-arhin@ug.edu.gh (D. Dodoo-Arhin).

https://doi.org/10.1016/j.matpr.2020.04.597
2214-7853/
Selection and peer-review under responsibility of the scientific committee of the International Symposium on Nanostructured, Nanoengineered and Advanced Materials.

able for purifying water with some amount of dye contaminants without yielding toxic intermediate products in most cases [10]. These semiconductor nanoparticles in the presence of light and at a specific wavelength can generate electron-hole pairs [11] which undergo series of oxidation and reduction reactions to produce hydroxyl groups as the main oxidizing agent to breakdown the organic components of the dye into green products [12]. A number of photocatalysts explored over the years include titanium dioxide (TiO_2), copper (II) oxide (CuO), zinc oxide (ZnO) and many others [13]. Amongst these catalysts, titanium dioxide has been widely used and explored in several studies owing to its photoactivity and ability to oxidize these dyes into green products [14] amidst some challenges such as low quantum effect and surface area [15].

However, zinc oxide in the light of the challenges posed by titanium dioxide is gradually gaining attention as a favourable alternative material for photocatalytic degradation of dye polluted water. This is because, it exhibits good photo activity and photo luminescence properties [16] with relatively high surface area and quantum yield compared to titanium dioxide [17]. It also has a high tendency of exhibiting high reaction and mineralization rates leading to the generation of hydroxyl ions which are the main oxidizing units [18].

Zinc Oxide is a heterogeneous n-type semiconductor material having a wide direct band gap of about ~3.37 eV and an exciton binding energy of ~60 meV [19]. With respect to its band gap energy, zinc oxide exhibits ultraviolet light (UV) absorption at room temperature and poor response to visible light in the electromagnetic spectrum. This restricts the intrinsic semiconductor to be used actively as a photocatalyst under a visible light source [4]. However, the bandgap of zinc oxide can be modified through p-type doping to increase its absorption spectrum into the visible light region [20]. Applications of ZnO span through various areas including catalysis, optoelectronics, gas and bio-sensors, active filler for rubber and plastic, UV absorbing agent in cosmetics and many more [21,22]. ZnO nanoparticles and powders with different surface morphologies and nanostructured geometries can be synthesized using simpler synthesis techniques including sol–gel, hydrothermal, precipitation, micro-emulsion synthesis, mechanochemical and combustion techniques [5,23].

In this study, synthesis of zinc oxide nanoparticles was carried out using the sol-gel technique. Augmented photocatalytic activity was achieved without the use of capping ligands. The photoactivity of zinc oxide nanoparticles at different calcination temperatures was explored by using it as a catalyst for the photo-induced degradation of Rhodamine B under UV light. Finally, the rate of degradation with increasing catalyst load was analyzed using Rhodamine B and the reusability of catalyst.

2. Experimental methods

2.1. Materials and chemicals

The reagents used in this work were Zinc acetate, Oxalic Acid, Ethanol (99%), Rhodamine B obtained from Loba Chemie Ltd (India). All the reagents used in this work were of analytical grade and were used as-received without additional purification.

2.2. Sol–gel synthesis of ZnO nanoparticles

ZnO nanoparticles were synthesized using the sol-gel method. In a typical experiment, ~0.01 mol of Zinc Acetate dehydrate was dissolved in 60 ml of absolute ethanol and stirred at 65 °C for 30 min to obtain a clear solution. Oxalic acid–ethanol solution was also prepared by dissolving 0.04 mol of oxalic acid dehydrate in 80 ml of ethanol and stirred for 30 min at 55 °C. The oxalic acid–ethanol solution was then added to the zinc acetate solution dropwisely at 65 °C and stirred continuously for 1 h. The resultant whitish solution was allowed to gel by ageing it for 2 h and subsequently dried at 80 °C in an oven for 24 h. The aerogel obtained was calcined at different temperatures: 400 °C, 500 °C and 600 °C for 5 h to obtain ZnO nanoparticles. Z_400, Z_500 and Z_600 were sample designations for ZnO nanoparticles calcined at 400 °C, 500 °C and 600 °C respectively.

2.3. Characterization of ZnO nanoparticles

To determine the phases present and the microstructure of the ZnO nanoparticles, powder X-ray diffraction (XRD) patterns were collected on an Empyrean diffractometer (Panalytical BV, Netherlands) with theta/theta geometry, operating a Cu-Kα radiation tube (λ = 1.5418 Å) at 40 kV and 45 mA. The XRD patterns of all the randomly oriented powder specimens were recorded in the 20°–80° 2θ range with a step size of 0.017° and a counting time of 14 s per step. The diffraction patterns were matched against the ICSD's PDF database and qualitative phase analysis conducted using the X'Pert Highscore plus search match software (Panalytical, Netherlands).

A high resolution FEI Nova NanoSEM 450 scanning electron microscope operated at 2.0 kV was used in the surface morphological investigations of the as-produced particles. Prior to the SEM analysis, the samples were metallized with carbon coating to render them conductive.

Transmission FTIR spectra were recorded on a PerkinElmer Spectrum Two™ FTIR Spectrometer in the 4000–400 cm^{-1} range with a 4 cm^{-1} resolution. Spectra were recorded and analysed with the Spectrum Touch software. UV–vis absorption spectroscopy was carried out on a GENESYS 10S UV–Vis spectrophotometer over a wavelength range of 200 nm–900 nm. The Tauc plot was used to estimate the band gap energy of zinc oxide nanoparticles. This was done by plotting a graph of $(\alpha h\nu)^2$ against $h\nu$ where $\alpha = \frac{2.303A}{d}$, A is the absorbance, d is the thickness of the material, h is Planck's constant and ν is the frequency of light absorbed.

2.4. Dye photocatalytic degradation experiment

Photocatalytic degradation experiments were carried out for the degradation of Rhodamine B under ultraviolet light illumination using ZnO nanoparticles as photocatalyst. A specially designed UV chamber was used for the experiment. 0.01 g/l Rhodamine B dye solutions were prepared using distilled water. A homogeneous mixture for each dye was obtained through stirring. A dye–catalyst mixture was prepared for each dye by adding 0.1 g of ZnO nanoparticles to 100 ml of each dye followed by rigorous stirring for 1 h in a dark room to enhance adsorption and desorption equilibrium reactions. Respective dye–catalyst mixtures were illuminated on a bench top Ultraviolet light source (UV transluminator, 330 W). Maximum illumination period was 160 min. The samples were swirled at every 5 min' interval whiles under illumination. About 3 ml of each sample was taken using a syringe at every 20 min' interval, centrifuged and the resulting supernatant analyzed by UV–vis spectrometry. Absorbance at wavelengths (λ_{max}) 555 nm and 665 nm was recorded for Rhodamine B. This experiment was carried out using Z_400, Z_500 and Z_600 to investigate the effect of crystallite size on the rate of photodegradation. ZnO nanoparticle dosage was varied from 0.1 g to 0.3 g for each dye with an interval of 0.05 g to investigate the effect of catalyst load on the rate of photodegradation.

3. Results and discussion

3.1. X-ray diffraction analysis

The X-ray diffraction (XRD) patterns as shown in Fig. 1 for Z_400, Z_500 and Z_600 samples gave a characteristic ZnO wurtzite structure with characteristic peaks at the following 2θ positions; 31.81°, 34.44°, 36.31°, 47.602°, 56.62°, 63.01°, 66.48°, 67.97°, and 69.19° corresponding to the (1 0 0), (0 0 2), (1 0 1), (1 0 2), (1 1 0), (1 0 3), (2 0 0), (1 1 2), and (2 0 1) planes, respectively for all samples [24]. The estimated crystallite size for all samples was calculated using the Debye Scherer equation: $D = \frac{K\lambda}{\beta\cos\theta}$ where k, the Scherer constant = (0.89), X-ray wavelength λ = (0.154 nm), Bragg's diffraction angle $\theta = 36.30^{\circ}$ corresponding to ZnO (1 0 1) reflection, and β, the Full Width at Half Maximum (FWHM) of the peak profiles for all samples were estimated using the Gaussian fitting.

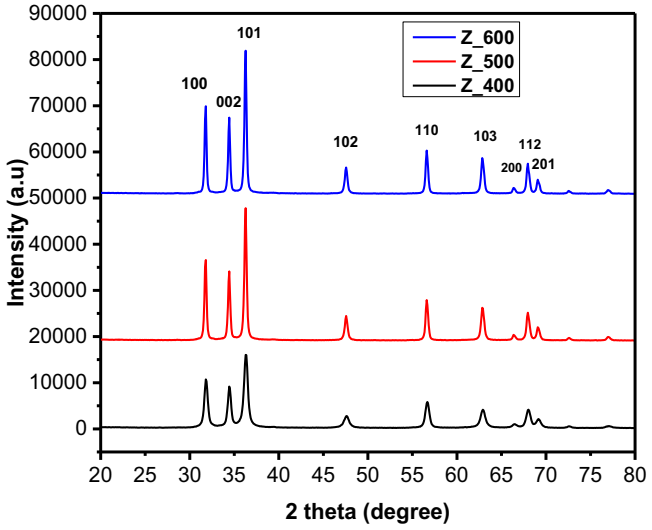

Fig. 1. XRD patterns of ZnO nanoparticles calcined at 400 °C, 500 °C and 600 °C.

Table 1
Crystallite size of ZnO nanoparticles at different calcination temperatures and their respective FWHM.

Calcination Temperature °C	Full width at Half maximum (FWHM)	Crystallite Size (nm)
400	0.544	16
500	0.314	28
600	0.290	30

The Table1 shows calculated values of the crystallite size of ZnO nanoparticles obtained at different calcination temperatures. ZnO nanoparticles calcined at 400 °C has the smallest crystallite size followed by samples calcined at 500 °C and 600 °C respectively. This trend indicates that an increase in temperature results in an increase in the crystallites of a material and hence an increase in grain size. Sharpness of peaks was also observed as calcination temperature was increased. This is as a result of increased crystallinity.

When the experimental XRD profiles were modelled using the Whole Powder Pattern Modelling (WPPM) technique incorporated in the PM2K software, a very low goodness of fit was obtained: an indication of a better fit between experimental and calculated data. The results of modelled XRD profiles are shown in Fig. 2a and b, respectively.

The domain size increased and broadened slightly as the calcination temperature was raised up to 400 °C, with the domain size distribution revealed to be between 1 nm and 15 nm. However, the domain size increased and broadened drastically over a wide size distribution when the calcination temperatures were increased to 500 °C.

Distribution of grains in ZnO particles as calcination temperature was increased was investigated by plotting the domain size against its frequency. This was done using the modelling tool. Results from the graph below shows that 14.2 nm domain size was predominant in Z_400, 32.0 nm in Z_500 and 42.0 nm in Z_600.

3.2. Fourier transform infra-red (FTIR) spectra

FTIR spectra of ZnO nanoparticles calcined at different temperatures (400 °C, 500 °C and 600 °C) are shown in Fig. 3. This characterization was done to determine the presence of zinc and oxygen molecules in the prepared zinc oxide nanoparticle and other functional groups that might be present. Fingerprint bands observed at 861 cm^{-1} and 688 cm^{-1} represent the inter-atomic vibrations of *Zn–O* bond. These bands are also characteristic of the metal zinc

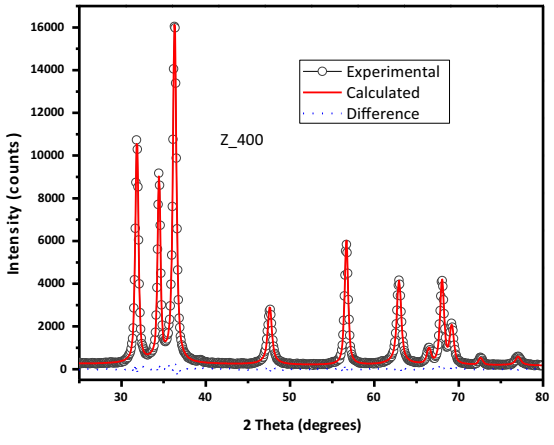

(a)

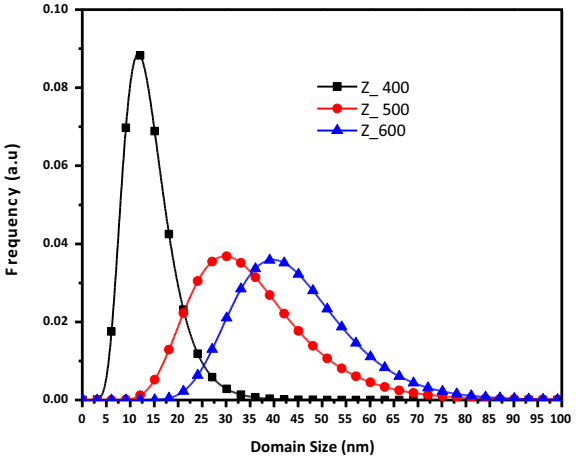

(b)

Fig. 2. Modelled XRD patterns of ZnO nanoparticles calcined at 400 °C and (b) lognormal size distribution of synthesized ZnO nanoparticles.

since bands of metals are usually observed below 1000 cm^{-1} [25]. The bands observed at 3400 cm^{-1}–3500 cm^{-1} are due to *O–H* hydroxyl group) bond stretching and deformation owing to the molecules of water adsorbed onto the surface of zinc. A decrease in the intensity of the band is observed as the calcination temperature was increased from 400 °C to 600 °C. This is an indication that more water molecules leave the sample at higher temperatures. Bands stretching from 2400 cm^{-1} to 1300 cm^{-1} represent *O═C═O* and *C═O* bonds as a result of carbon dioxide adsorption from the atmosphere during synthesis [26,27]. It is also observed that there is a negligible shift to a lower wavenumber due to increase in the calcination temperature. This shift can be related to a change in the lattice parameters of the ZnO nanoparticles [28].

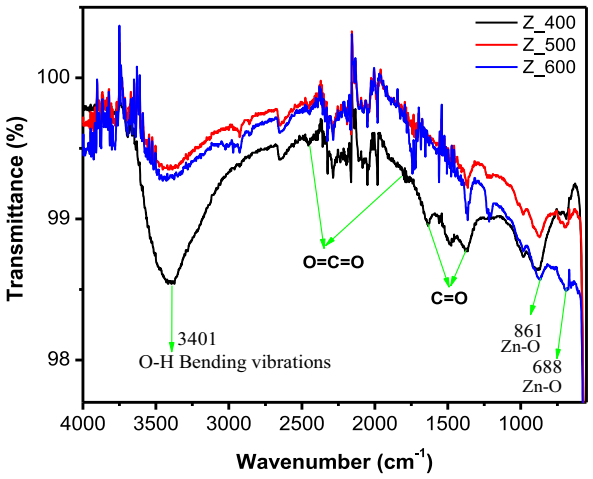

Fig. 3. FTIR Spectra of ZnO nanoparticles.

3.3. Scanning electron microscopy (SEM)

The SEM (*see* Fig. 4) micrograph obtained for the various samples portrayed fibrous (rod-like) morphological structures with considerable particle agglomeration. With increase in the calcination temperatures, the level of agglomeration increased as seen for particles calcined at 600 °C showing the most agglomeration (Fig. 4c). Particle agglomeration could be attributed to the high nucleation and grain growth rate at higher temperatures. This observation is consistent with the increased in crystallinity and grain sizes observed from the x-ray diffraction analysis in Section 3.2. Nanoparticles with very small crystallite size and less agglomeration possess large surface area (*active sites*) which tends to enhance photocatalytic reactions.

3.4. Optical band gap estimation from UV–Vis spectra

From the UV–vis spectra in Fig. 5a, the bandgap energy of the synthesized ZnO nanoparticles were estimated using the Tauc Plot (Fig. 5b). A graph of $(\alpha h\upsilon)^2$ *against* $h\upsilon$ was plotted, where α is the absorption coefficient of the material. The absorption coefficient is the amount of radiations absorbed by the material with respect to its thickness. The absorption coefficient: $\alpha = \frac{2.303A}{d}$, where A is the absorbance and d is the thickness of the material. A tangent to the curve is extrapolated to the *x*-axis to read the band gap energy of ZnO nanoparticles as shown in Fig. 5b. The tangent was taken at the point where the curve begins to linearize.

A decrease in bandgap energy was observed for ZnO nanoparticles as the calcination temperature was increased from 400 °C to 600 °C. This is attributed to the increase in the vibrational amplitude of electrons at higher temperatures. It can also be attributed to quantum size effect where smaller crystallite size materials have high confinement of electrons in the energy levels resulting in an increase in the band gap [25]. Therefore, band gap energy for ZnO nanoparticles increases with decreasing crystallite size due

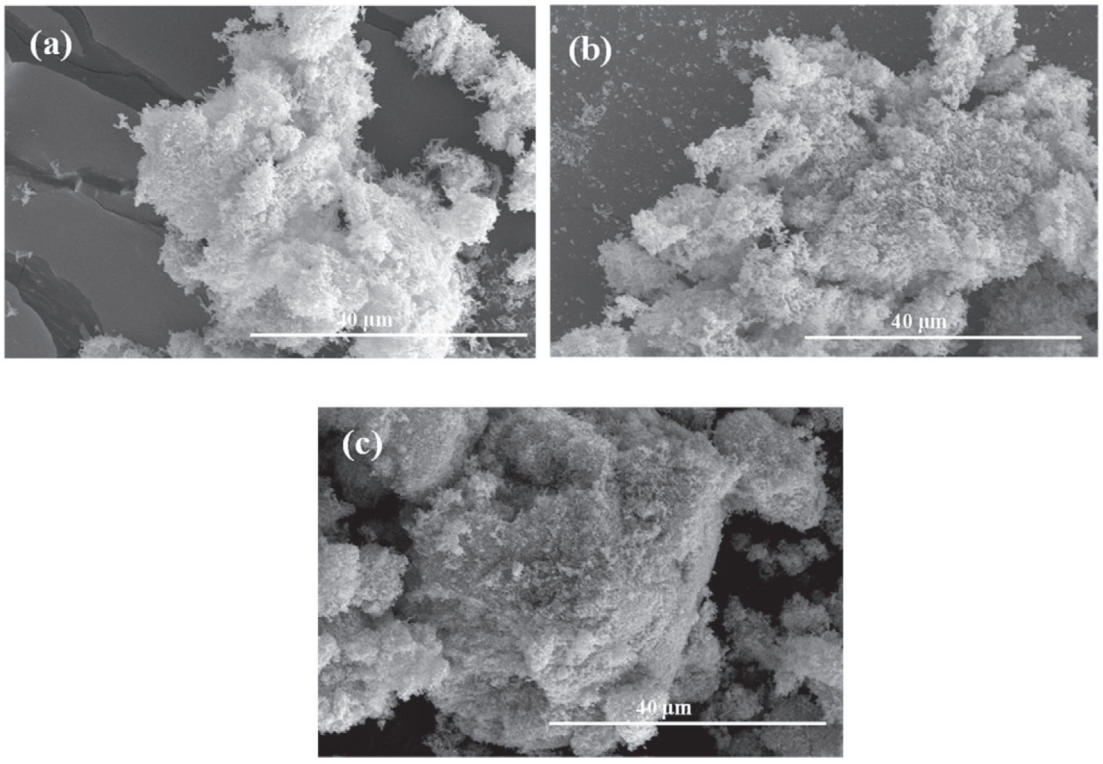

Fig. 4. SEM images of ZnO nanoparticles calcined at (a) 400 ℃, (b) 500 ℃, (c) 600 ℃.

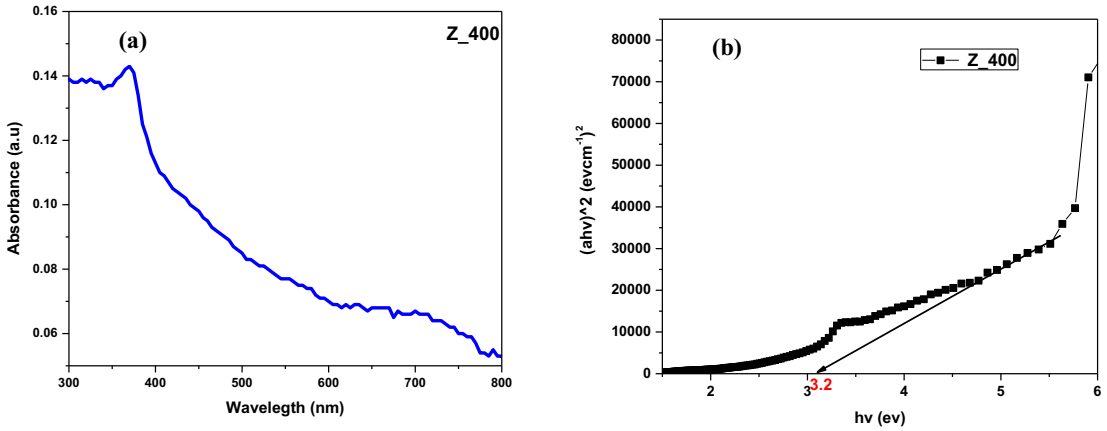

Fig. 5. (a) UV–Vis Spectrum and (b) Classical Tauc plot of Zinc Oxide nanoparticles synthesized at 400 °C.

to quantum size effect and decreases with increasing temperature due to electrons vibrational amplitude.

3.5. Photocatalytic degradation of Rhodamine B

Photocatalytic degradation of the Rhodamine B dye was carried out with the use of zinc oxide nanoparticles in the presence of ultraviolet light from a UV transluminator of 330 W. Results from the UV–vis spectrometry analysis during photocatalytic degradation experiment are shown in Fig. 6. The degradation of the dye (Fig. 6a) was marked successful based on the observations that the initial concentrations of the dye in the solution decreased resulting in the decolourization of the solutions after UV illumination for 160 min. Dye–catalyst solutions did not undergo degradation without UV illumination (Fig. 6b) likewise no degradation of non-catalyst dye solution under illumination (Fig. 6c). This is an

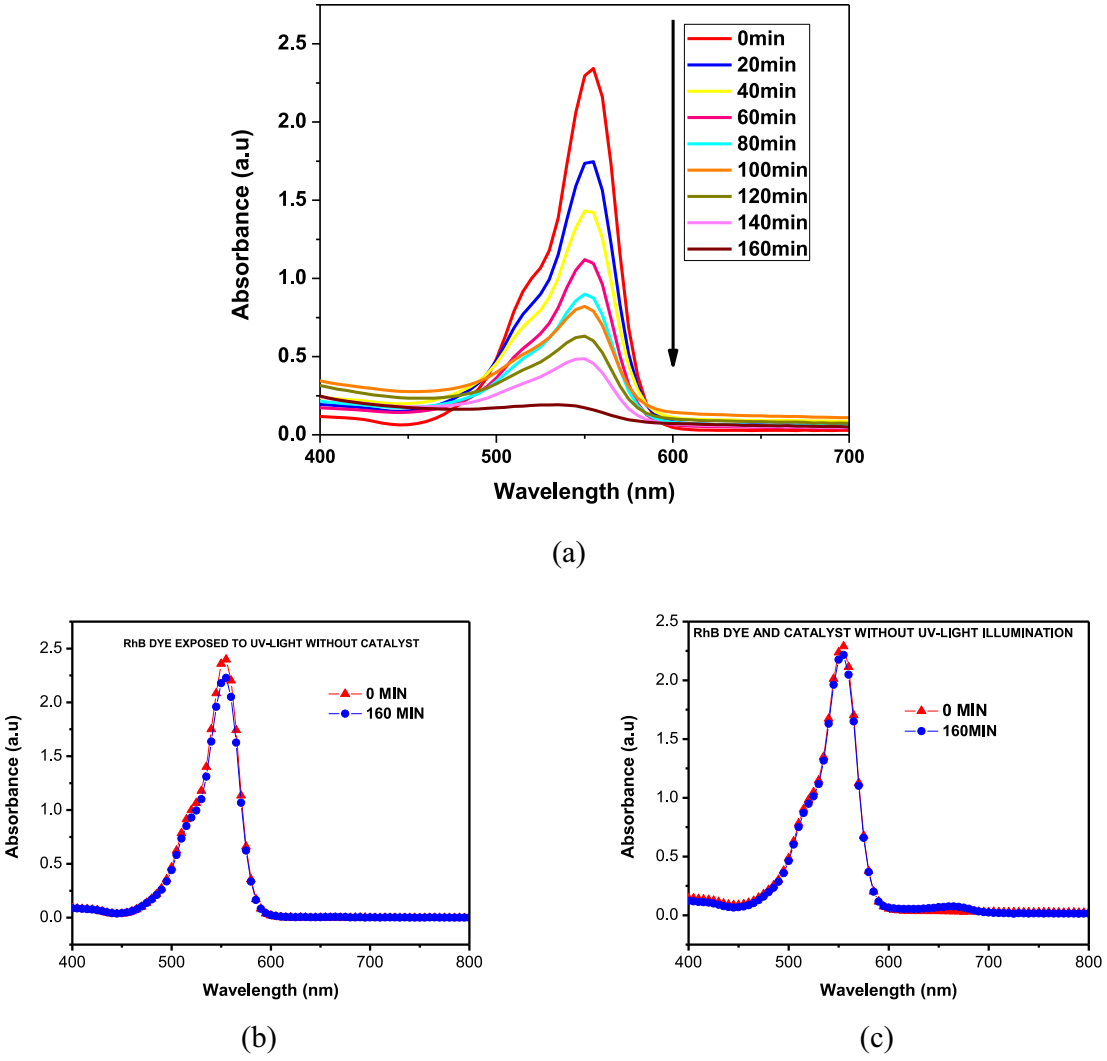

Fig. 6. Rhodamine B (a) degradation with catalyst under UV light irradiation, (b) without catalyst under UV light irradiation and (c) with catalyst but no UV light illumination.

indication that degradation of dye concentrates in the solution is solely due to photocatalytic reactions.

The reaction mechanism for the degradation is shown below:

ZnO particles are photoinduced to generate electron–hole pairs, as shown in Eq. (1) when illuminated with light of photon energy greater than the bandgap energy of ZnO.

$$ZnO + h\nu \rightarrow (e^{-}_{(CB)}) + (h^{+}_{(VB)}) \quad (1)$$

The electron–hole pairs generated by photo-excitation undergo redox reactions as shown in Eqs. ((2)–(4)) below. The holes (h^+ ions) undergo series of oxidation reactions with water to release hydroxide ions and subsequently into hydroxyl radicals (Eqs. (2) and (3)). Electrons, e^- reduces oxygen into superoxide radical (Eq. (4)) and subsequent reactions between superoxide radical and H^+ ions generate several hydroperoxyl compounds which combine together to form hydrogen peroxide (Eqs. (5) and (6)) [11].

$$(h^{+}_{(VB)}) + H_2O \rightarrow H^{+} + OH^{-} \quad (2)$$

$$(h^{+}_{(VB)}) + OH^{-} \rightarrow OH\cdot \quad (3)$$

$$(e^{-}_{(CB)}) + O_2 \rightarrow O_2^{\cdot -} \quad (4)$$

$$O_2^{-} + H^{+} \rightarrow HO_2\cdot \quad (5)$$

$$HO_2\cdot + HO_2\cdot \rightarrow H_2O_2 + O_2 \quad (6)$$

Further reaction between hydrogen peroxide and superoxide radicals results in the generation hydroxyl radicals as shown in Eq. (7). Excess hydrogen peroxide is also converted into hydroxyl radicals in the presence of light as shown in Eq. (8) below:

$$H_2O_2 + O_2^{\cdot -} \rightarrow OH\cdot + OH^{-} + O_2 \quad (7)$$

$$H_2O_2 + h\nu \rightarrow 2OH\cdot \quad (8)$$

The hydroxyl radicals released are the main oxidizing agents that break down complex organic pollutants adsorbed on the ZnO and convert them into intermediate products and subsequently into green products such as water and carbon dioxide as shown in Eqs. ((9) and (10)) [29].

$$\text{Organic pollutants} + OH\cdot \rightarrow \text{Intermediates} \quad (9)$$

$$\text{Intermediates} \rightarrow CO_2 + H_2O \quad (10)$$

Therefore, ZnO nanoparticles (catalyst), in the presence of light generated electron–hole pairs which migrate to its surface to initiate the reactions. Hydroxyl radicals and superoxide radicals are produced when holes combine with hydroxyl groups and electrons combine with oxygen on the surface of the catalyst respectively. The radicals constitute the major species that oxidize the Rhodamine B into green products such as carbon dioxide, water and mineral acids.

3.6. Effects of catalyst crystallite size and loading on dye degradation

Photocatalytic degradation of Rhodamine B was carried out using ZnO nanoparticles of different crystallite sizes to investigate the effect of different crystallite size on the rate of degradation. The rate of degradation was calculated as the amount of dye degraded within 160 min. Nanoparticles having the smallest crystallite size showed the highest degradation rate of the dyes. This is due to the existence of large surface area (*more reactive sites*) for increased photocatalytic reactions. Nanoparticles with the smallest crystallite size were achieved at 400 °C calcination temperature. The amount (%) of dye degraded is give as:

$$d(\%) = \frac{C_O - C_t}{C_o} \times 100 \quad (11)$$

where C_O is the initial concentration of the dye and C_t is the concentration of the dye at a particular irradiation time. The amount of catalyst used in the photodegradation process was varied from 0.1 g to 0.3 g with an increment of 0.05 g to determine its effect on the dye degradation. For every catalyst load, the volume of dye was maintained at 100 ml. Zinc oxide nanoparticles calcined at 400 °C were used in this experiment. A graph of the amount of dye remaining against time of irradiation is shown in Fig. 7 for the various catalyst load. It was observed that, photodegradation increased as catalyst load was increased from 0.1 g to 0.2 g and eventually decreased for 0.25 g and 0.3 g catalyst load.

Catalyst load of 0.3 g recorded that lowest dye degradation after 160 min as it comes with the highest amount of dye remaining as shown in Fig. 7 whereas the highest photodegradation was observed for 0.2 g catalyst load as it shows the lowest amount of dye remaining in 160 min. This makes the 0.2 g catalyst load the optimum amount for the degradation of the dyes. The obtained results compare well with literature values [4,30] even though capping ligands were not used in this present work.

The increase in catalyst load from 0.1 g to 0.2 g, increased the number of ZnO active sites resulting in the absorption of more light photons and high adsorption of dye molecules and hence an increase in the rate of photocatalytic reaction to degrade the dyes. However, a decrease in the photodegradation of the dyes was observed as the catalyst load increased from 0.25 g to 0.3 g due

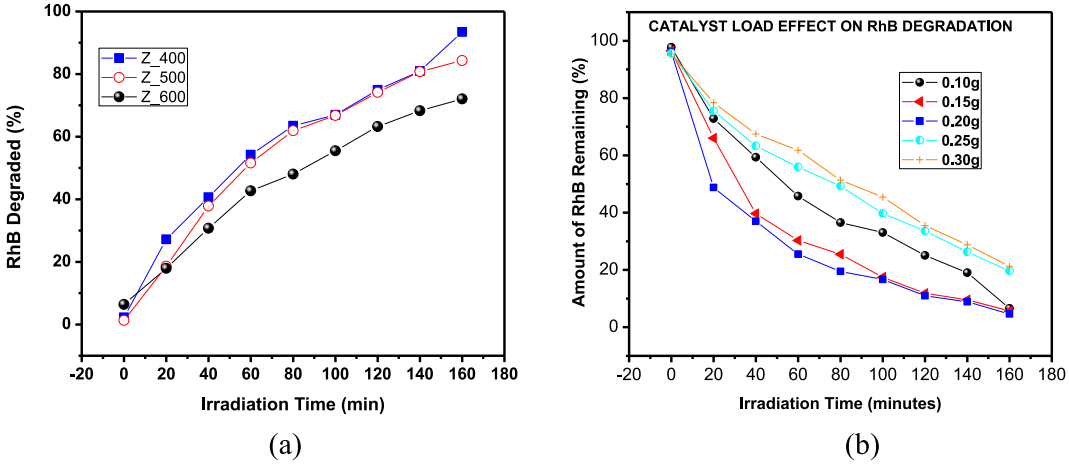

Fig. 7. (a) Amount of RhB degraded against time and (b) Catalyst load effect on RhB degradation.

to the presence of excess ZnO nanoparticles which inhibited the penetration of light and hence reduced the amount of photons absorbed.

4. Conclusion

Zinc oxide nanoparticles were synthesized using the sol-gel method. Various characterization methods, including XRD, FTIR, SEM and UV–vis spectrometry have been used to substantiated the formation and presence of ZnO NPs. The Microstructure, crystalline nature and the existence of specific functional groups were confirmed by XRD and FTIR. The effect of temperature on the crystallite sizes, energy bandgap and photocatalytic activities of the nanoparticles have been explored. The fibrous nanorod-like morphology of the particles provided a larger surface area and reactive sites for photocatalysis. The as prepared ZnO nanoparticles were used as a photocatalyst to degrade Rhodamine B dye with an optimum catalyst load of 0.2 g and efficiency of 95.41% degradation of within 160 min. Hence, sol-gel is a preferred method in attaining higher photocatalytic activity of ZnO nanostructures for the removal of various organic contaminants from wastewater. This study offers a low-cost eco-friendly solution to water purification.

CRediT authorship contribution statement

D. Dodoo-Arhin: Conceptualization, Methodology, Formal analysis, Writing - original draft. **T. Asiedu:** Conceptualization, Methodology, Investigation, Writing - original draft. **B. Agyei-Tuffour:** Conceptualization, Writing - review & editing. **E. Nyankson:** Writing - review & editing. **D. Obada:** Writing - review & editing. **J.M. Mwabora:** Writing - review & editing.

Declaration of Competing Interest

The authors declare that they have no known competing financial interests or personal relationships that could have appeared to influence the work reported in this paper.

Acknowledgements

The African Materials Science and Engineering Network (AMSEN); Regional Initiative on Science and Education (RISE); University of Ghana BANGA-Africa programme and University of Ghana Biotechnology Centre are duly acknowledged for their support.

References

[1] E.A. El-Sharkawy, A.Y. Soliman, K.M. Al-Amer, J. Colloid Interface Sci. 310 (2) (2007) 498–508.
[2] V. Jadhav, P. Chikode, G. Nikam, S. Sabale, Mater. Today:. Proc. 3 (10) (2016) 4121–4127.
[3] R. Saleh, N.F. Djaja, Superlattices Microstruct. 74 (2014) 217–233.
[4] A. Balcha, O.P. Yadav, T. Dey, Environ. Sci. Pollut. Res. 23 (2016) 25485–25493.
[5] M. Blue, B.G. Ankamwar, V.B. Kamble, J.I. Annsi, L.S. Sarma, C.M. Mahajan, J. Nanosci. Nanotechnol. 17 (2) (2017) 1185–1192.
[6] H. Zollinger, in: Color: A Multidisciplinary Approach, first ed., 2006, pp. 1–258.
[7] S.S. Vieira, Z.M. Magriotis, N.A.V. Santos, M.das G. Cardoso, A.A. Saczk, Chem. Eng. J. 183 (2012) 152–161.
[8] H.X. Guo, K.L. Lin, Z.S. Zheng, F. Bin Xiao, S.X. Li, Dye Pigm. 92 (3) (2012) 1278–1284.
[9] H. Kyung, J. Lee, W. Choi, Environ. Sci. Technol. 39 (7) (2005) 2376–2382.
[10] M.R. Hoffmann, S.T. Martin, W. Choi, D.W. Bahnemann, Chem. Rev. 95 (1) (1995) 69–96.
[11] C.B. Ong, L.Y. Ng, A.W. Mohammad, Renew. Sustain. Energy Rev. 81 (1) (2018) 536–551.
[12] R. Ameta, M.S. Solanki, S. Benjamin, S.C. Ameta, Photocatalysis (2018).
[13] S. Gardin et al., J. Phys. Chem. C 114 (17) (2010) 7646–7652.
[14] L. Chen et al., Ceram. Int. 35 (8) (2009) 3275–3280.
[15] A.N. Wang, Y. Teng, X.F. Hu, L.H. Wu, Y.J. Huang, Y.M. Luo, P. Christie, Sci. Total Environ. 541 (2016) 348–355.
[16] S.M. Lam, J.C. Sin, A.Z. Abdullah, A.R. Mohamed, Desalin. Water Treat. 41 (1–3) (2012) 131–169.
[17] E.R. Carraway, A.J. Hoffman, M.R. Hoffmann, Environ. Sci. Technol. 28 (5) (1994) 786–793.
[18] S. Baruah, M. Jaisai, R. Imani, M.M. Nazhad, J. Dutta, Sci. Technol. Adv. Mater. 11 (5) (2010).
[19] X. Zhang et al., J. Phys. Chem. C 119 (35) (2015) 20544–20554.
[20] S. Majumdar, P. Banerji, Sens. Actuators B: Chem. 140 (1) (2009) 134–138.
[21] A. Kolodziejczak-Radzimska, T. Jesionowski, Materials (Basel) 7 (4) (2014) 2833–2881.
[22] Y.T. Chung, M.M. Ba-Abbad, A.W. Mohammad, N.H.H. Hairom, A. Benamor, Mater. Des. 87 (2015) 780–787.
[23] A.C. Mohan, B. Renjanadevi, Proc. Technol. 24 (2016) 761–766.
[24] X. Chen, Z. Wu, D. Liu, Z. Gao, Nanoscale Res. Lett. 12 (1) (2017) 4–13.
[25] H. Kumar, R. Rani, Int. Lett. Chem. Phys. Astron. 19 (2013) 26–36.
[26] Z.R. Khan, M.S. Khan, M. Zulfequar, M.S. Khan 2011 (2011) 340–345.
[27] A.B. Lavand, Y.S. Malghe, J. Asian Ceram. Soc. 3 (3) (2015) 305–310.
[28] K. Zak, M.E. Abrishami, W.H.A. Majid, R. Yousefi, S.M. Hosseini, Ceram. Int. 37 (1) (2011) 393–398.
[29] M. Klare, J. Scheen, K. Vogelsang, H. Jacobs, J.A.C. Broekaert, Chemosphere 41 (3) (2000) 353–362.
[30] T. Varadavenkatesan, E. Lyubchik, S. Pai, A. Pugazhendhi, R. Vinayagam, R. Selvaraj, J. Photochem. Photobio. B: Biol. 199 (2019) 111621.